Weihua Zhao · Xilin Xia · Xiaoli Su · Qiuhua Liang · Xiuwei Liu · Nengpan Ju

Movement process analysis of the high-speed long-runout Shuicheng landslide over 3-D complex terrain using a depth-averaged numerical model

Abstract Flow-like landslide is one of the most catastrophic types of natural hazards due to its high velocity and long travel distance. In 2019, a large catastrophic landslide was triggered by heavy rainfall and occurred in Shuicheng County, Guizhou, China. The Shuicheng landslide was characterized by a short slip time, high speed, and long sliding distance, causing significant damages to the downstream communities and properties. Depth-averaged models have been widely used to predict the velocity and runout distance of flow-like landslides. However, most of the existing depth-averaged models have various shortcomings for application in real-world simulations. In this study, a high-performance depth-averaged model taking into account the effects of topography-related vertical acceleration and centrifugal force was used to examine the influence of complex 3-D terrain on the landslide movement process. The simulation results were in satisfactory agreement with the field observations. This work reveals the landslide movement process at different stages, including acceleration, diversion, secondary acceleration, impact, and deposition. The maximum average velocity was predicted to be 35 m/s, with a local maximum velocity exceeding 50 m/s. The seismic records obtained from the adjacent seismic stations and the predicted kinetic energy and velocity of the landslide event revealed a dual acceleration and obstruction process. It was also found that the movement process and final deposit morphology were strongly influenced by the complex terrain and were sensitive to the surface friction coefficient. This may also be the reason for the survival of some houses in the middle of the slope during the event. This study provides a reference for investigating long-runout, high-speed, flow-like landslides.

Keywords Shuicheng landslide · Movement process · Terrain effect · Friction coefficient sensitivity · Seismic wave

Introduction

Flow-like landslide is one of the most catastrophic types of natural hazards owing to its high velocity and long travel distance (Hungr et al. 2014). Many large-scale landslide events, such as the Mount Meager rock slide-debris flow in Canada on August 6, 2010 (Guthrie et al. 2012), the Oso landslide in the USA on March 22, 2014 (Iverson et al. 2015), and the Xinmo landslide in Sichuan, China, on June 24, 2017 (Fan et al. 2017; Hu et al. 2018), were characterized by a high-speed, long-runout distance, and flow-like movement. These landslides move in a manner dynamically similar to fluids after initiation and can travel a much longer distance than that is predicted by simple frictional models (Legros 2002). The high mobility renders such landslides highly hazardous (Yin and Xing 2012; Watkins et al. 2015).

Numerical models have been widely used to predict the dynamics of flow-like landslides and to quantify the runout distance and

flow velocity to facilitate risk assessment and management. Owing to their simplified formulation and lower computational cost compared with the full 3D models, depth-averaged models have been successfully developed and applied to simulate granular flows (Savage and Hutter 1989), including flow-like landslides (Pudasaini et al. 2007; Gray and Edwards 2014; Iverson and George 2014; George and Iverson 2014). For geophysical granular flows, such as avalanches, landslides, and debris flows, a challenging task of the depth-averaged models is to simulate real-world events and account for the effects of complex 3-D topographies. Attempts have been reported to address this challenge by introducing certain hypotheses or simplifications. Gray et al. (1999) and Pudasaini and Hutter (2003) assumed that the flow direction was parallel to the domain surface and subsequently adopted a surface-fitted curvilinear coordinate system in their depth-averaged models. Bouchut and Westdickenberg (2004) and Mangeney et al. (2007) introduced a shallow water flow model on an arbitrary coordinate system to support simulations over topographies with small curvatures. To utilize a global Cartesian coordinate system while maintaining solution accuracy, Juez et al. (2013) and Hergarten and Robl (2015) simply modified the original governing equations by including a projection factor for the pressure and source terms, determined by the bed or surface topography gradients according to heuristic geometric arguments. However, most existing depth-averaged models still have limitations when they are applied to simulate real-world simulations. To correctly account for the effects of large slope gradients and curvatures and allow users to take advantage of raster-based DEM data, Xia and Liang (2018) presented a new depth-averaged model based on a global coordinate system for simulating field-scale flow-like landslide, which included extra terms in the governing equations to account for the effects of vertical acceleration and centrifugal force caused by complex terrain topographies.

The Shuicheng landslide, which occurred suddenly at the night of July 23, 2019, buried 21 houses, caused 51 casualties or missing people, and injured 11 others. In less than 2 min, approximately 2 million m^3 of cataclastic basalt soil failed, with a runout of approximately 1.25 km over a total vertical distance of approximately 465 m. To better understand the potential mechanisms that caused the high-speed and long-runout behavior of the landslide, Zhao et al. (2020) conducted a detailed post-event field survey and performed a preliminary analysis of the movement characteristics. The landslide area possesses some unique 3-D terrain features, including three platforms and two gullies. The sliding mass was split into two parts during the event, and three houses survived in the middle of the slope.

In this study, we examine the effect of complex 3-D terrain on the movement process of Shuicheng landslide using a high-

performance depth-averaged model. The simulation results are compared with field geological surveys to verify the model. This study provides a detailed reference for analyzing the motion of high-speed long-runout landslides in real complex 3-D terrains.

Overview of the Shuicheng landslide

Following a detailed field survey, a preliminary analysis was undertaken to understand the geological background, deformation history, and geological characteristics of the Shuicheng landslide event. The landslide area is mainly located in the Emeishan Formation (P_{2-3}em) with a basaltic lithology, covered with a thin layer of soil. Figure 1 shows the overall terrain before and after the event. Three platforms (P1, P2, and P3) and two gullies (G1 and G2) were identified in the landslide area (Fig. 1a). The bottom of the area is a valley depression. The landslide area can be generally divided into three zones (Fig. 1b), i.e., the source area, entrainment area, and deposit area. Three houses survived on the ridge between the two gullies (Fig. 1c). The relative elevation difference was approximately 465 m between the source and deposition areas, and the maximum travel distance in the main sliding direction was approximately 1250 m.

Historical remote sensing images, InSAR results, and geological monitoring data did not identify any notable signs of deformation before the landslide (Zhao et al. 2020). The landslide was induced by heavy rainfall and suddenly occurred over a short period. According to the Guizhou Meteorological Bureau (2019), between July 18 and 23, the landslide area experienced three periods of heavy rain shortly before the landslide, respectively, in the night of July 18, from July 19 to July 20, and in the night of July 22. The cumulative rainfall at this site reached 189.1 mm for July 18–23 and 98 mm for July 22–23.

Figure 2 shows some of the geological phenomena observed at the site after the landslide in the source area. The bedrock of the main scarp (a long joint surface) can be identified at the back edge of the landslide (Fig. 2(c)) and below the scarp to the road, as part of the landslide body deposition. On the ridge behind the surviving houses, debris shunting features can be clearly detected (Fig. 2(d)). Figure 2(e) shows the characteristics of the debris in the gully G1 bend, with movement along and over the gully, causing damage to and burial of houses. These geological phenomena indicate that the landslide was characterized by fast movement, as shown in Fig. 2(a, b). After the landslide body was detached, it fell onto the lower platform, disintegrated rapidly, and generated a high-speed debris flow along gullies G1 and G2, which collapsed and buried the houses near the gullies. The landslide eventually converged and deposited at the bottom. A high-speed long-runout landslide is often accompanied by strong microseismic phenomena, and the generated vibrations can be recorded by the nearby seismic networks (Ekstrom and Stark 2013; Zhou et al. 2016; Zhang et al. 2019). Some villagers in Jichang Town 1 km away from the site recalled the rumbling sound — "like thunder" — they heard during the landslide. This indicates that a strong tremor occurred during the landslide.

The method reported by Scheidegger (1973), which is the most common method for estimating the velocity of high-speed landslides and debris flows, was used to calculate the movement velocity of this landslide. The results (Fig. 3) show that the velocity of the sliding body continued to increase rapidly after initiation due to a decrease in altitude and the transfer of potential energy into kinetic energy, and reached a maximum speed of 35.7 m/s. The flow velocity began to decrease sharply as the terrain becomes flattened. From start to finish, the landslide movement lasted for approximately 50 s.
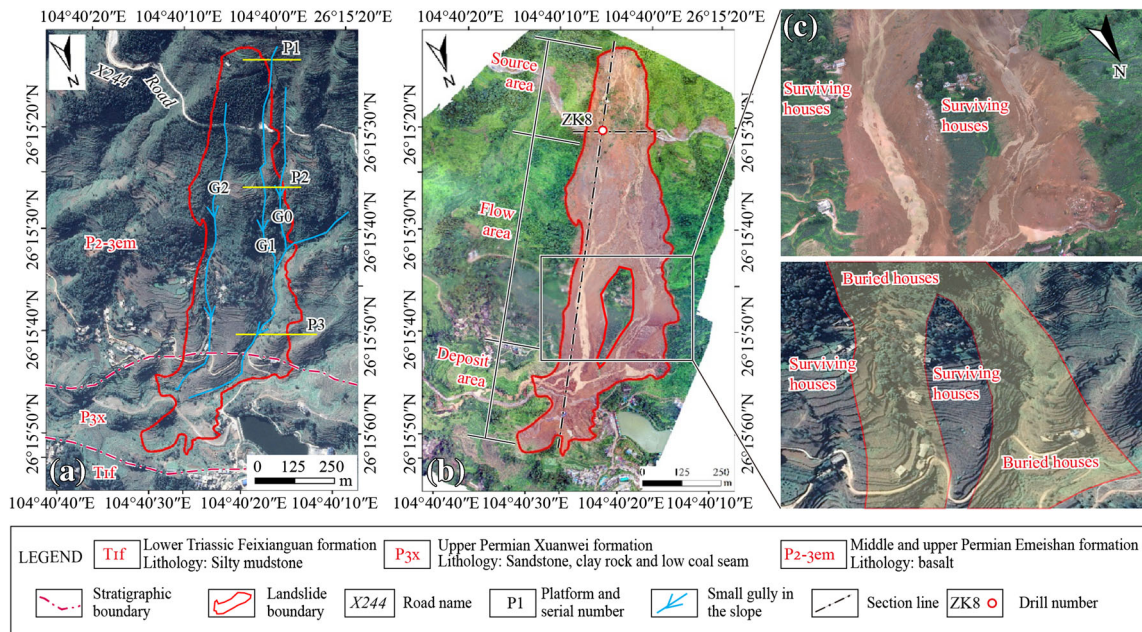

Fig. 1 Pre- and post-sliding images of the Shuicheng landslide site: **a** Google Earth terrain image before the slide (December 31, 2016); **b** aerial image after the slide (July 25, 2019); and **c** main area where houses were buried or survived
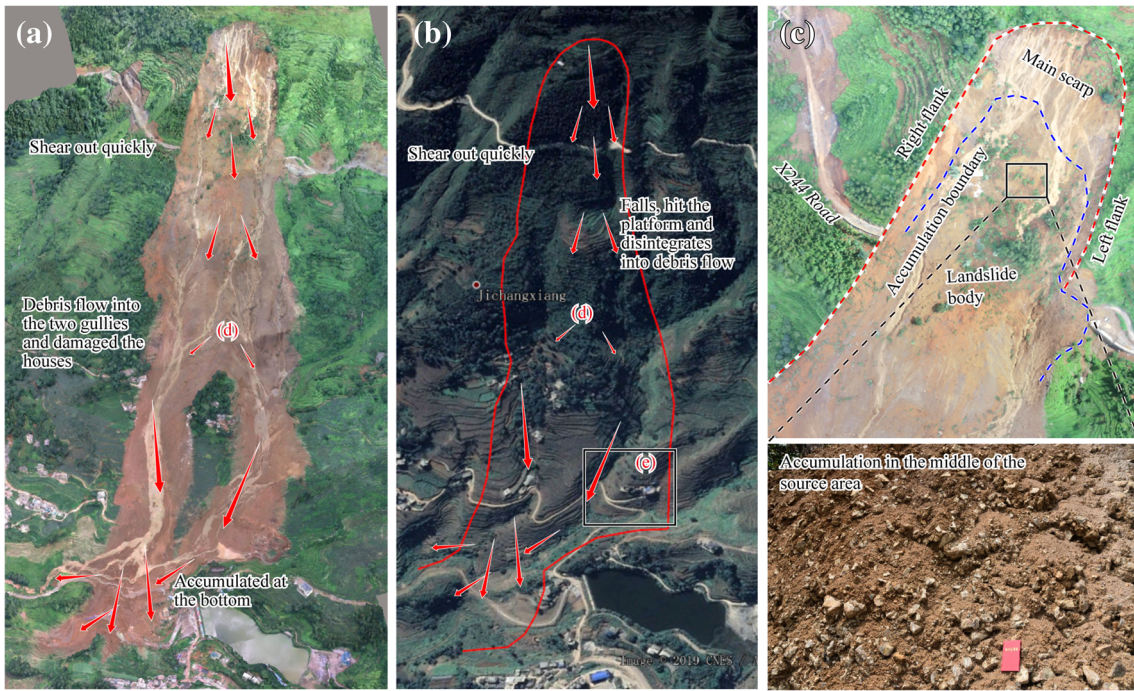
Fig. 2 Possible movement process of the landslide (a and b) and some of the geological phenomena that occurred during the high-speed debris flow and its strong impact; (c) bedrock of the main scarp and part of the deposited landslide material; (d) debris shunting features behind surviving house; (e) debris flow at the gully G1 bend

Numerical model and parameters

Numerical methods of the adopted depth-averaged model

A depth-averaged model reported in Xia and Liang (2018) was used to calculate the movement process and 3-D topography of the flow-like landslide. In this model, the depth-averaged equations were derived from the three-dimensional governing equations by assuming Mohr–Coulomb rheology, and the final depth-averaged equations are written in matrix form as

$$\frac{\partial \boldsymbol{q}}{\partial t} + \frac{\partial \boldsymbol{f}(\boldsymbol{q})}{\partial x} + \frac{\partial \boldsymbol{g}(\boldsymbol{q})}{\partial y} = S_b + S_f, \tag{1}$$

where the vector terms are as follows:

$$\boldsymbol{q} = \begin{bmatrix} h \\ uh \\ vh \end{bmatrix} \quad \boldsymbol{f}(\boldsymbol{q}) = \begin{bmatrix} uh \\ u^2h + \frac{1}{\varnothing^2}\frac{1}{2}gh^2 \\ uvh \end{bmatrix} \quad \boldsymbol{g}(\boldsymbol{q})$$

$$= \begin{bmatrix} vh \\ uvh \\ v^2h + \frac{1}{\varnothing^2}\frac{1}{2}gh^2 \end{bmatrix}, \tag{2}$$
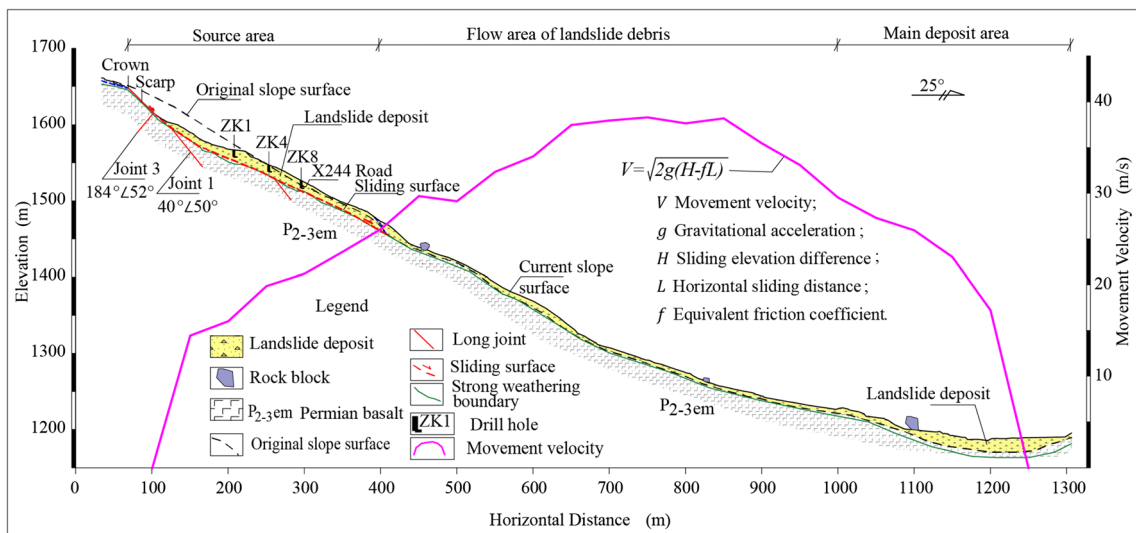

Fig. 3 Longitudinal geological section (along the sliding direction as shown in Fig. 1) and the movement velocity estimated using the Scheidegger (1973) method

$$S_b = \begin{bmatrix} -ah\dfrac{\partial b}{\partial x} + \dfrac{1}{2}gh^2\dfrac{\partial(1/\varnothing^2)}{\partial x} \\ -ah\dfrac{\partial b}{\partial y} + \dfrac{1}{2}gh^2\dfrac{\partial(1/\varnothing^2)}{\partial y} \end{bmatrix} \quad S_f$$

$$= \begin{bmatrix} \dfrac{\overset{0}{\mu ahu\varnothing}}{\sqrt{u^2 + v^2 + \left(u\frac{\partial b}{\partial x} + v\frac{\partial b}{\partial y}\right)^2}} \\ \dfrac{\mu ahv\varnothing}{\sqrt{u^2 + v^2 + \left(u\frac{\partial b}{\partial x} + v\frac{\partial b}{\partial y}\right)^2}} \end{bmatrix}, \tag{3}$$

$$a = \frac{1}{\varnothing^2}\left(g + V^THV\right), \text{ in which } V = (u,v)^T, H$$

$$= \begin{bmatrix} \dfrac{\partial^2 b}{\partial x^2} & \dfrac{\partial b}{\partial x \partial y} \\ \dfrac{\partial b}{\partial x \partial y} & \dfrac{\partial^2 b}{\partial y^2} \end{bmatrix}, \text{and} \tag{4}$$

$$\varnothing = \left\{\left(\frac{\partial b}{\partial x}\right)^2 + \frac{\partial b^2}{\partial y} + 1\right\}^{1/2}, \tag{5}$$

where t is time, (x, y) defines two-dimensional Cartesian coordinates, g is the acceleration due to gravity, h is the flow depth, b is the bed elevation, and u and v are the x depth-averaged velocities in the x- and y- directions, respectively. The above equations appear to be similar to the shallow water equations, which may be beneficial in terms of directly adopting existing numerical methods originally developed for solving the shallow water equations. But compared with conventional shallow water equations, in addition to the friction terms, there are three major differences:

Firstly, the gravity terms have an additional factor $1/\varnothing^2$ that reduces the gravity effect. This factor is only related to the bed topography but is independent of both of the coordinate system and the velocity direction. This factor is essential in ensuring the rotational invariance of the above depth-averaged equations. The inclusion of this factor is theoretically important for the governing equations to properly describe the effects of complex topography in a Cartesian coordinate system.

Secondly, the V^THV term is included to account for the effect of centrifugal force. The centrifugal force may increase the normal pressure, and hence, the friction force, such that the movement predicted by the new equations, may become slower. The inclusion of centrifugal force can also predict a faster flow movement in certain situations than that predicted by the models that do not consider curvature effect. Explicitly including the centrifugal force will retain the magnitude of velocity as centrifugal force only changes the direction of the flow.

Finally, the second terms, i.e., $\frac{1}{2}gh^2\frac{\partial(1/\varnothing^2)}{\partial x}$ and $\frac{1}{2}gh^2\frac{\partial(1/\varnothing^2)}{\partial y}$, in Eq. (3), are included to mathematically preserve the landslide body at rest conditions. Numerical experiments demonstrate that neglecting these terms may lead to inaccurate predictions when attempting to reproduce experimental granular flows.

Similar formulations have been reported in the literature (e.g., Juez et al. 2013; Hergarten and Robl 2015), but they do not include the new centrifugal force term and other extra terms in Eq. (3) and the resulting model may be less robust for real-world applications involving complex terrain features. Compared with other more complicated Boussinesq-like models (e.g., Denlinger and Iverson 2004; Castro-Orgaz et al. 2014), the model solving the current depth-averaged governing equations is computationally much less demanding because of the use of a simpler formulation and subsequently the requirement of less sophisticated numerical schemes. Although they are derived based on the Mohr–Coulomb rheology, the new governing equations can be easily incorporated with friction laws with varying coefficients, such as the velocity-dependent friction law proposed by Pouliquen and Forterre (2002). In principle, they can also be extended to include more complex two-phase rheologies. In order to further improve its performance for large-scale real-world simulations, the model is further implemented on multiple graphics processing units (GPUs) to achieve high-performance computing (refer to Xia et al. (2019) for details).

Terrain data and material parameters

The focus of this study was to simulate and understand the dynamic movement process after the landslide is initiated using a physically based model. The detailed information about the depth distribution of the landslide body and the terrain of the slide bed was required to set up the model. LiDAR data was available at a resolution of 1.0 m for the area below the local county road X244 to cover the main landslide movement domain after its initiation. However, high-resolution terrain data above the county road was not available, and so the open SRTM worldwide elevation data (3-arc-second resolution) is used to cover the area above the county road.

Figure 4 shows the pre-event terrain data from the last merged data. After the landslide occurred, several boreholes (ZK1 to ZK13 in Fig. 4d) were made inside the landslide. Drilling can help reveal the sliding surface (H2) after a landslide, and then the terrain difference before and after the landslide (E1-E2) can be calculated to estimate the depth of the sliding body. In this way, the depth of the sliding body at the 14 borehole locations was obtained. Finally, assuming, which 0-m depth at the landslide boundary, the depth contour map of the slide body in the slide source area was obtained by interpolation, as shown in Fig. 4 c. The terrain of the sliding bed (Fig. 4b) was derived by subtracting the depth of the landslide body from the terrain data acquired before the event.

According to the field survey, the landslide body material was mainly composed of highly weathered basalt, crushed block, and clay, with a relatively loose structure. The slide-belt material remaining on the back wall proved that the basalt gradually became soft and muddy when it was saturated with groundwater, with notable frictional shear characteristics evidenced by local scratches. To determine the shear strength parameters of the geotectonic materials, a large cross-section test box of $15 \times 15 \times 15$ cm was used for undisturbed sampling of the material in the sliding zone, and a shear test on the undisturbed sample was carried out in the laboratory. The material parameters of the sliding belt material and landslide body were obtained and listed in Table 1. The natural density, cohesion, and internal friction angle were used to set up the adopted depth-averaged model for
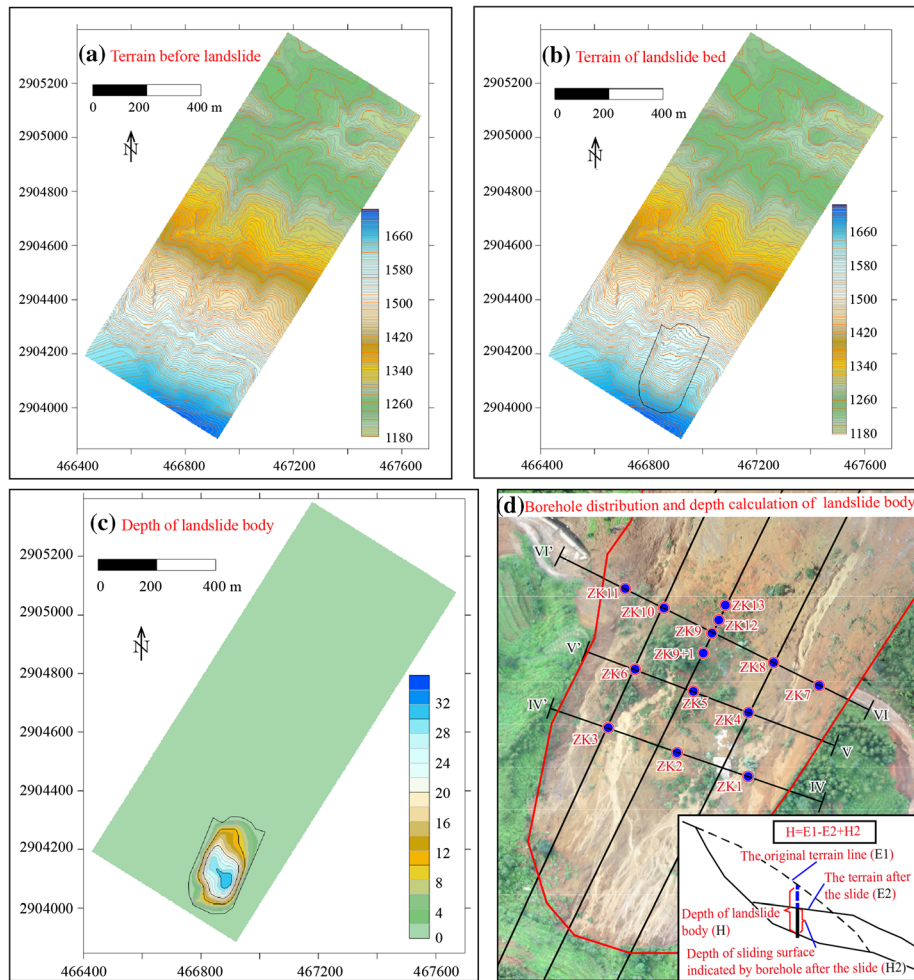
Fig. 4 Terrain (a) before and (b) after the landslide (without the landslide deposit and landslide body), (c) depth of the landslide body, and (d) distribution of boreholes and depth calculation of the landslide body

the following simulations. In addition, the friction coefficient of the slope surface was set to 0.43 in the model.

Numerical results

Comparing the numerically predicted morphology with field data

To verify the predictive capability of the model, we compared the simulated landslide morphology with the UAV orthophoto image taken after the landslide (Fig. 5). Certain specific areas ((a–f in Fig. 5) were also selected for a more detailed comparison.

(1) Deposit at the intersection of the left boundary of the landslide and the road (position (a) in Fig. 5): The landslide deposit at this point is unexpected because it is located outside the overall boundary of the landslide (dashed line in Fig. 6). Based on Fig. 6, the stepladder formed by the road excavation did not deform, but the slide body, with a thickness of 3–4 m, was deposited below. Moreover, the slide body overturned a car from the road to its position on the retaining wall below the road. The numerical simulation reproduced the deposit characteristics. At position (a) (simulation result on the left in Fig. 5), there is a bulging heap. The formation of this mound is discussed in the analysis of the landslide process below.

(2) Characteristics of the landslide along the road (Fig. 5(b)): Figure 7 shows a cross-sectional diagram near the road after the landslide. The borehole indicates that the thickness of the

Table 1 Physical and strength parameters of the materials in the landslide source area

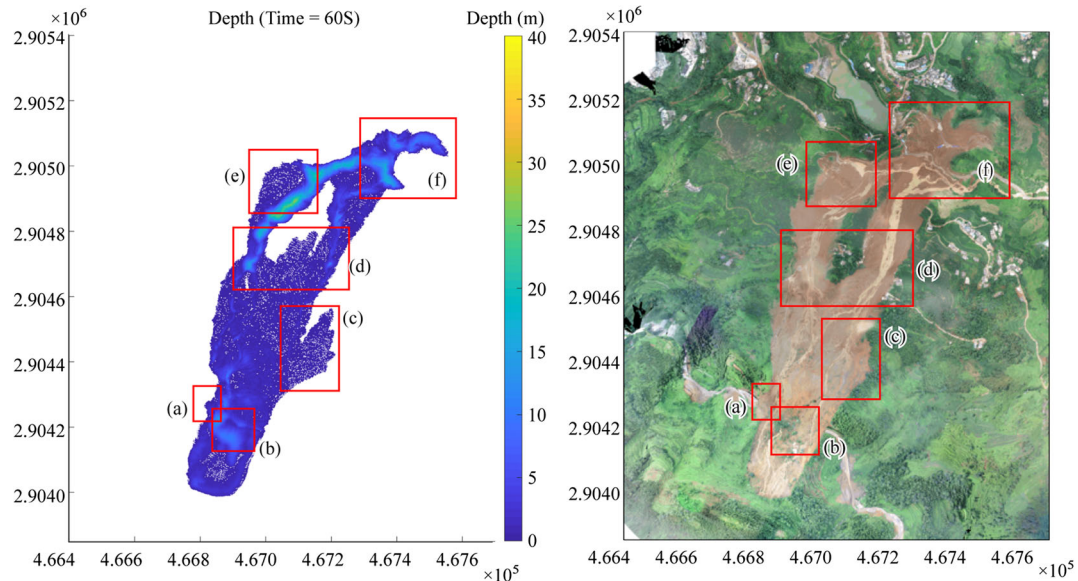| Material	Natural density (g/cm³)	Saturated density (g/cm³)	Cohesion (KPa)	Internal friction angle (°)
Landslide body	2.44	2.46	93.8	23.5
Sliding belt	1.67–1.79	1.71–1.83	63	23.5

Fig. 5 Comparison between the predicted final morphology (left) and the UAV orthophoto image taken after the landslide (right); (a)–(f) show detailed comparison in specific locations

landslide deposit body was approximately 15 m, showing that a major deposit area formed around the road. The results of the model simulation also show that there was a concentrated deposit with a larger depth in this area (i.e., area (b) in the landslide UAV image in Fig. 5).

(3) Figure 8 shows photos taken after the landslide in areas (c) and (d) in Fig. 5. Based on Fig. 5, the simulation results of (c) and (d) were similar to the overall landslide site morphology, but slightly different in their size of the distribution area. The extent of the landslide in area (c) predicted by the model was larger than the observation. In location (d), compared with the landslide site, the area in the middle (where survived houses are located) was predicted to be relatively large in width but relatively small in the longitudinal direction, and the sliding body moved close to the trailing edge of the survived houses. Based on Fig. 8, there was a large number of thick trees at the site in both areas, which may have caused a significant difference in the friction coefficient of the slope surface in these two areas compared with that in other places. The uniform slope friction coefficient adopted in the numerical model does not reflect this and may be the reason for the slight deviation from the observation.

(4) Areas (e) and (f) in Fig. 5 are the main deposit areas of the landslide. Figure 2(e) shows that the landslide caused damage to the houses on the slope and also casualties. Figure 5(e) shows that the numerical simulation results were consistent with the field observations. The simulated morphology shown in Fig. 5(f) was also overall consistent with the field data.

Flow velocity and depth during the entire landslide movement process
Figures 9 and 10 show the simulated flow velocity and depth, respectively, to reveal the movement and deposit process of the

landslide after initiation. The entire landslide movement process was divided into the following stages.

(1) Initiation of the landslide and overall downward movement of the landslide body (at approximately 5 s): After its initiation in the source area, the sliding body exhibited an overall downward movement trend. As shown in Fig. 9, at 5 s, the slide body at the middle and rear edge pushed the slide body at the front forward. A small part of the slide body first moved into the left gully.

(2) Rapid acceleration stage after landslide initiation, i.e., shear out (at approximately 10 s): As shown in Fig. 9, the flow velocity at 10 s shows that, although the slide body still had overall dynamic characteristics at this time and the velocity of the leading edge increased significantly, the velocity of the trailing edge had already started to decrease relatively to its initial movement. The front edge of the slide was curved, with a trend of moving in the downward direction. The depth (thickness) of the slide body was also larger in the middle and anterior parts, and a relatively larger amount of material flowed into the left gully (yellow area in Fig. 10 at 10 s).

(3) The sliding body accelerated rapidly along both sides of the channel, and the middle ridge part bifurcated to both sides (at approximately 15 s). At 15 s, the sliding body was mainly concentrated in the gullies on both sides (G0, G1, and G2 in Fig. 1); the materials moving to the middle ridge were also separated into the gullies on both sides due to the topographic effect, and G0 finally transformed into G1. The depth of the material in the two gullies was greater than that in the other parts. In this process, the houses in the vicinity of Fig. 5(d) were destroyed by sliding material moving at a high velocity, and some residents were buried or injured.

(4) Continued rapid movement to the bottom and gradual deposit stage (at 20–30 s): In this stage, the slide continued to move at a high speed, causing considerable damage, and the velocity at the
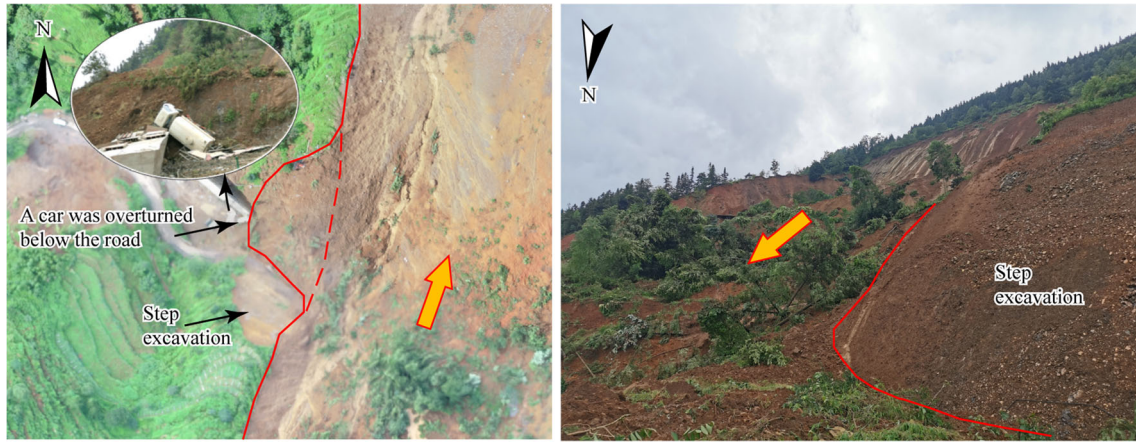
Fig. 6 Landslide deposit characteristics at the intersection of the left boundary of the landslide and the road (position (a) in Fig. 5)

bottom gradually decreased with increasing downward deposition. This process had the following characteristics.

① Figure 6 shows the cause of deposition at this location. According to the slide depth at 20–25 s as shown in Fig. 10, deposition appeared on the road on the left side of the landslide. This may be due to the special bottom sliding surface and slope topography. The left surface gully (G1) is rich in material. In addition, in a previous study (Zhao et al. 2020), we reported that the bottom slide surface of the landslide was controlled by a long steep structural surface on the upper part and a wavy gentle surface on the lower part. The orientation of the long structural plane is 30°∠46°, and its dip direction has a small angle with a main sliding direction of approximately 20°. Therefore, at the bottom of the landslide, an intersection line inclined in the NW direction formed, and the intersection line on the left side of the landslide extends to just above the road. Therefore, part of the landslide material moved along the NW intersection line and formed a small deposit outside the landslide boundary (Fig. 11).

② The landslide caused damage to houses and casualties of residents at low elevations. As shown in Fig. 12, channel G1 has notable turning characteristics. When the slide material moved along the gully, its movement was blocked, which led to the deceleration of one part of the slide material with continued movement along the gully, while the other part of the slide material turned over the gully, forming a slope flow. Although the velocity of the flow on the slope decreased, it still reached up to 20–30 m/s, which caused the collapse and destruction of several houses located on the slope; the people inside these houses were removed by the sliding body and buried at a low elevation.

③ This indicates the material source and deposition process of the special morphology of multiple bifurcations at the bottom. This particular form was controlled by the complex terrain. In addition to the two gullies in which the landslide travelled, two small circular hills were located at the bottom. The flow velocity diagrams at the bottom for 22, 24, and 28 s are supplemented in Fig. 13. In these figures, material in the right channel (G2) first rushed to the bottom at 20–24 s and then flowed in the direction of (2-a), (2-b), and (2-c), as shown in Fig. 14. Material in channel G1 then reached the bottom and combined with the G2 material, which flowed in both directions with part of the G2-derived material and deposited.

(5) A small amount of sliding material continued to flow from the top to bottom in the channels, followed by a decrease in movement, which formed the final deposit (30–50 s). In Fig.
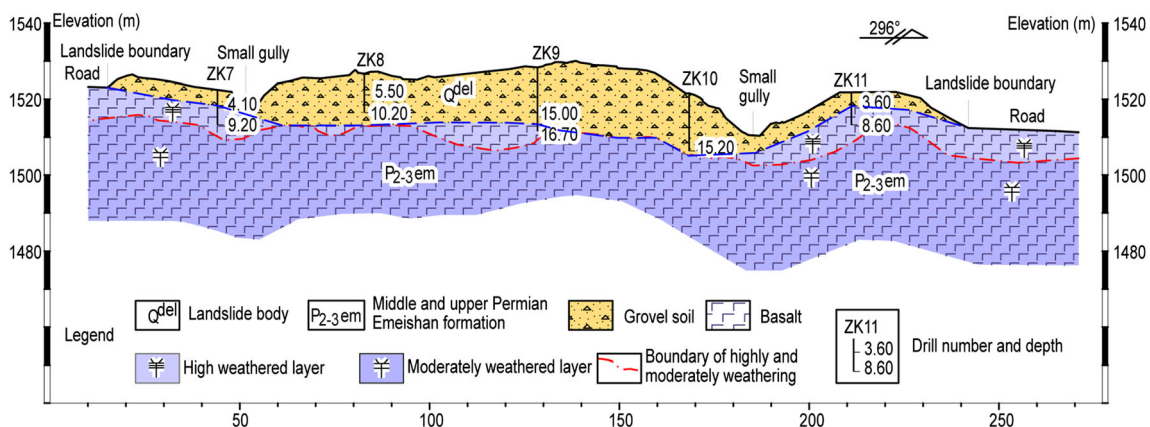

Fig. 7 Transverse section near the road after the landslide (roughly perpendicular to the direction of the slide), which is one of the main deposit areas of the landslide

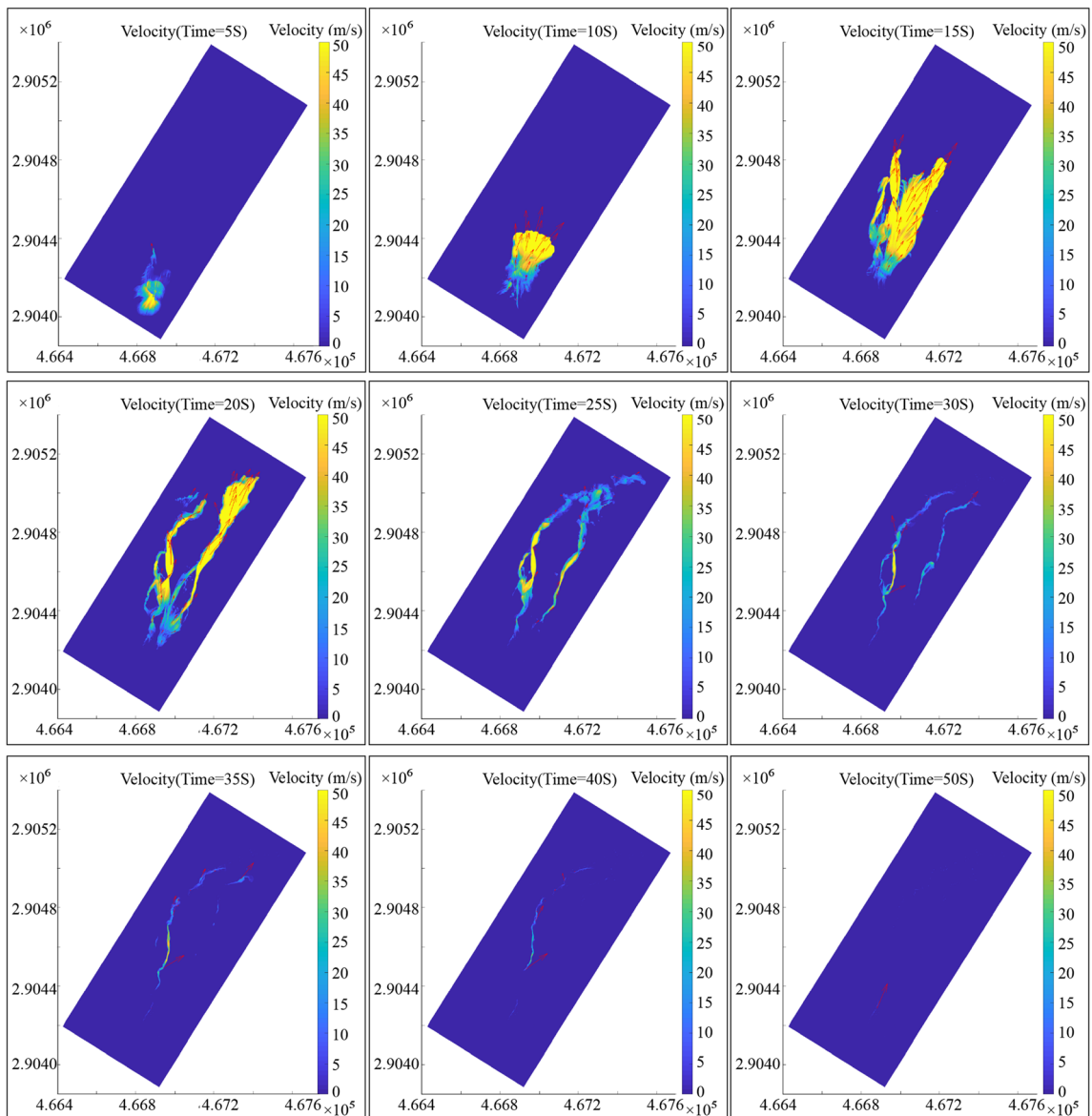**Fig. 8** Landslide distribution and surface vegetation of areas (c) (left) and (d) (right) in Fig. 5

Fig. 9 Simulated flow velocity at different output times during the landslide
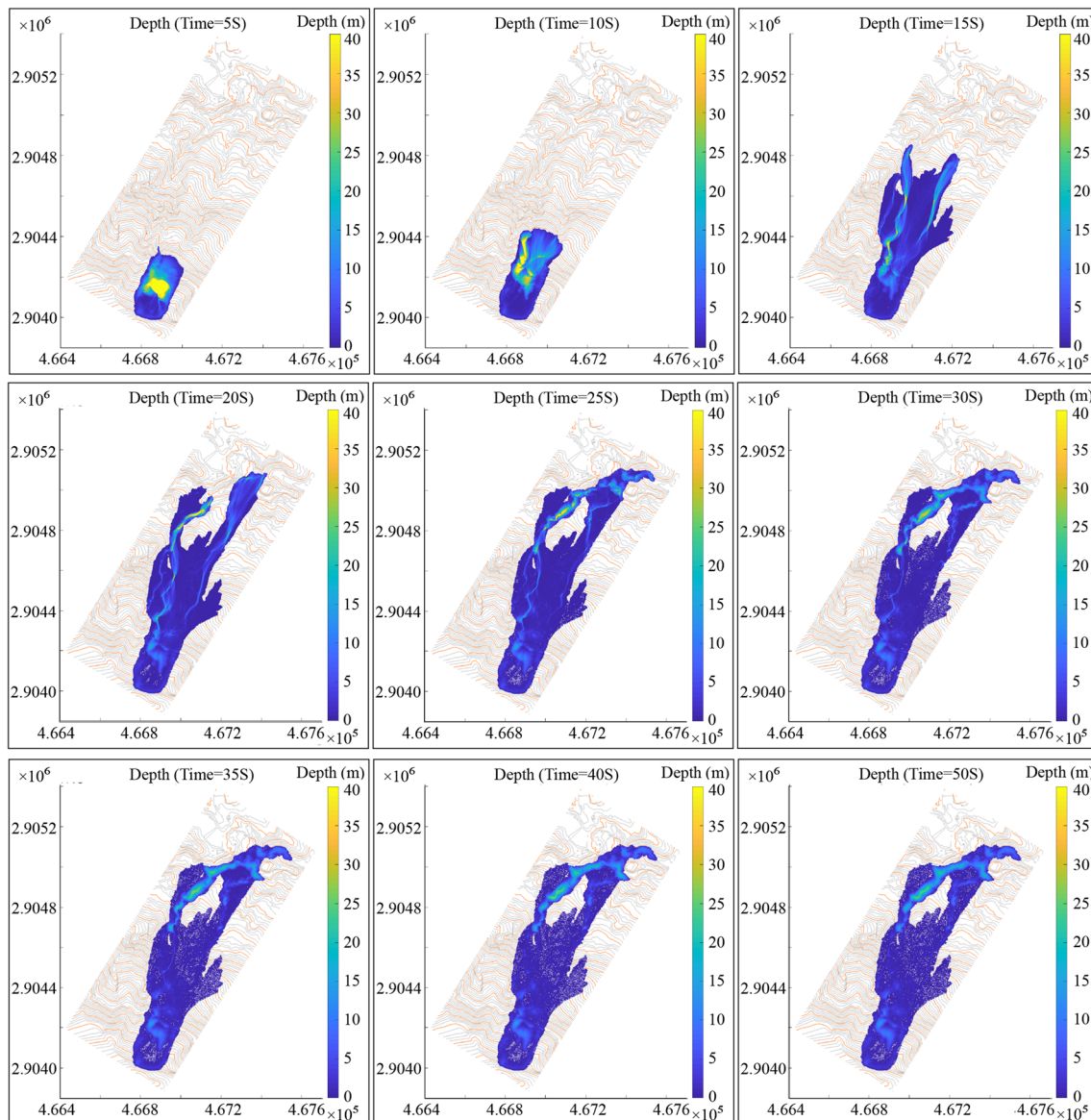
Fig. 10 Simulated flow depth at different output times during the landslide

10, after 30 s, the thickness of the landslide deposition has remained largely unchanged, indicating that the overall movement of the landslide had essentially settled. However, in the velocity diagram shown in Fig. 9, there was still a small amount of sliding material that flowed along the channels, especially in the left channel (G1). The flow rate then gradually decreased with gradual downward deposition, forming the final deposit.>

Discussion

Comparison between the predicted movement process and seismic wave records

From the field investigation and numerical simulation, we reconstructed the process at the initiation, sliding, disintegration, deposition, and impact stages of the Shuicheng landslide, which involves complex physical and mechanical mechanisms. Some villagers in the nearby Jichang town recalled that when the landslide happened, "It was like thunder. The rumbling sound was very horrible." (Zhao et al. 2020). This indicates that there was a strong tremor when the landslide occurred.

The landslide was recorded by the adjacent seismic stations. Figure 15 a and b show the horizontal east–west and vertical velocity of seismic waves at 120 s recorded by a station before and after the occurrence of the landslide. The fluctuation in seismic waves can reflect the movement process of the landslide. In the seismic wave, fluctuations were notable between approximately 35 and 70 s, which may be interpreted as the landslide movement time, i.e. approximately 35 s. The vigorous motion stage of the landslide occurred between the two red dotted lines (lasting for approximately 15 s), and two peaks appeared at 55 and 61 s.
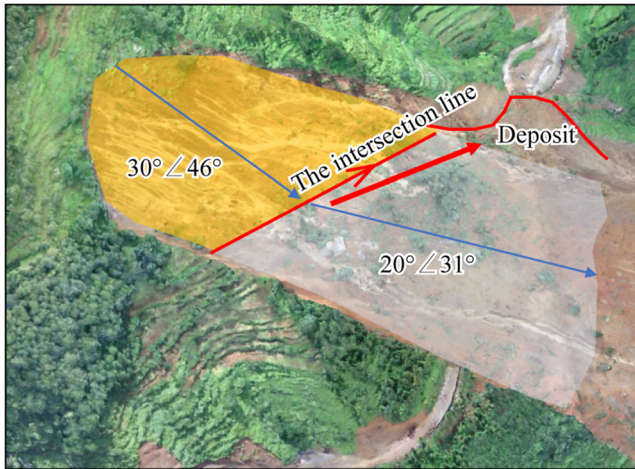
Fig. 11 Diagram of the possible causes of deposition at the location shown in Fig. 6

In this study, we numerically simulated the movement process of the landslide after its initiation. The previously presented velocity and depth maps revealed that the intense movement of the landslide lasted for approximately 30 s. To further analyze dynamic change of landslide movement, Fig. 15 c shows the kinetic energy calculated through $E = \sum \frac{1}{2}\rho \times$ Grid area $\times$ Depth$^*v^2$. The results show that the kinetic energy was comparatively large between 3 and 20 s, peaked at 6 and 14 s, but was relatively low at 10 s. The turning points of the kinetic energy curve are consistent with the trends in the observed seismic waves.

In addition, the change in the kinetic energy is well consistent with the landslide process. After the landslide was initiated, both of the velocity and kinetic energy increased rapidly, leading to the first peak. Then, the kinetic energy decreased when the landslide reached platform P2 in Fig. 1 at 10 s. Subsequently, the landslide material flowed into the gullies on both sides at a rapidly increasing volume, and the kinetic energy also increased accordingly.

From this analysis, it effectively showed that the intense movement of landslides may trigger and be recorded by seismic waves, providing an alternative source of data for analyzing landslide dynamics in the future. This comparative analysis also further verified the capability of the adopted model for simulating flow-like landslides.

For further comparison, Guo et al. (2020) also reproduced the Shuicheng landslide and investigated the terrain effect on the landslide dynamics using a model solving the shallow water equations without considering the effects from vertical acceleration and centrifugal force. They produced satisfactory results for the final deposit morphology of the landslide. However, the movement process of landslide predicted by their model was approximately 190 s, and the predicted time histories of velocity were different from the seismic wave records and the simulation results obtained in this study. This confirms the importance of accounting for the effects of vertical acceleration and centrifugal force in the simulation of real-world landslide events over complex terrains and that the adopted depth-averaged model is potentially more suited for practical applications.

Sensitivity of friction parameters

As previously mentioned, the simulated morphology of the landslide in Fig. 5(c, d) is slightly different from the field observation. This may be due to the thick vegetation cover (trees) on the slope surface, which may cause local variations in the surface friction in the various landslide areas. Herein, we further investigate and discuss the sensitivity of modelling results to different friction coefficients. The friction coefficient used in the original landslide simulation was 0.43. By varying the slope friction coefficient between 0.39 and 0.49, more simulations were run and the resulting final deposition forms of the landslide are shown in Fig. 16. Although the friction coefficient varied by only 0.1, large difference was detected in the simulation results, demonstrating the potential sensitivity of the simulation results to the friction coefficient.

When the friction coefficient was set to less than 0.43, i.e., either 0.41 or 0.39, the deposition thickness of the landslide near the road (blue
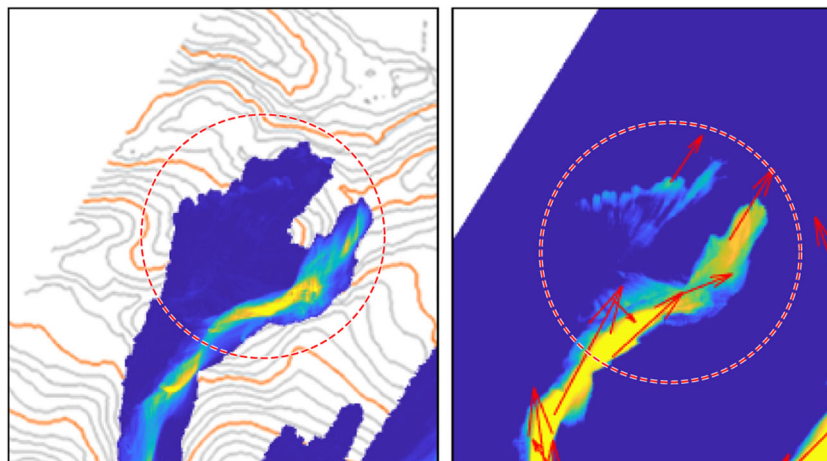

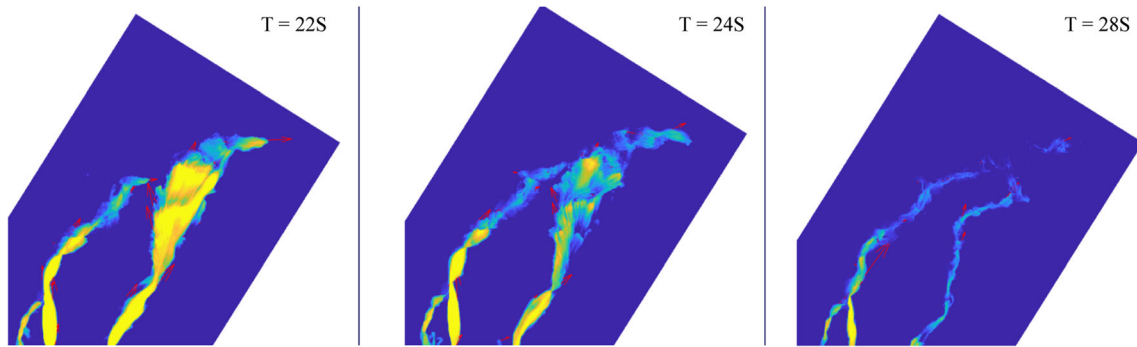**Fig. 12** Fast-moving slides caused damage to houses and casualties in the area shown in Fig. 5(e)

Fig. 13 Flow velocity characteristics of the debris at 22, 24, and 28 s at the bottom

dashed line) was relatively small, whereas at the bottom (red dotted line), the landslide material tended to spread out, and the majority of the deposition was piled up in the bottom ditch. However, when the friction coefficient gradually increased beyond 0.43, the landslide mainly deposited near the road and in the two trenches, neither flowing to the bottom, nor causing casualties in the area shown in Fig. 5(e). However, regardless of the friction coefficient, the landslide formed a vacancy in the middle part, i.e., the survival area (the area shown in Fig. 5(d)). Therefore, from a parameter sensitivity analysis perspective, the reason for the survival of the houses was mainly topographic control and local vegetation effects. As a summary, whilst the modelling results are shown to be sensitive to the surface friction coefficient, the complex terrain is the main controlling factor of the movement process and final deposition morphology of the Shuicheng flow-like landslide.

Conclusions

The 2019 Shuicheng landslide was a rapid and long-runout landslide devastating the downstream communities. Field investigations suggested that the terrain played an important role in the movement process of the landslide. In this study, a depth-averaged model considering the effects of vertical acceleration and centrifugal force was used to investigate the influence of 3-D complex terrain on the landslide movement process in detail. Based on the

simulation results and analysis, the following conclusions may be drawn:

1) The complex movement process was reproduced by the model and the predicted final morphology of the landslide was consistent with the field observation. The landslide movement process could be divided into several stages: (1) the landslide was initiated, followed by overall rapid acceleration; (2) a small part of the landslide was deposited near the road (shear exit), with divergence to both sides; (3) a second acceleration in the two gullies, which impacted houses; and (4) deposition at the bottom. The average velocity of the landslide was up to 35.7 m/s, with a local maximum velocity exceeding 50 m/s.

2) The landslide was recorded by the nearby seismic stations. From the seismic records, the violent movement of the landslide lasted for approximately 35 s, which was consistent with the numerical prediction. Seismic records may provide an alternative source of data for future analyses of landslide movements.

3) Survived houses were protected by the particular terrain features and the trees behind these houses. This study also proved that for a flow-like landslide, terrain setting is the controlling factor for the movement process and final deposition morphology of the landslide, although the simulation results were also shown to be sensitive to the surface friction coefficient.
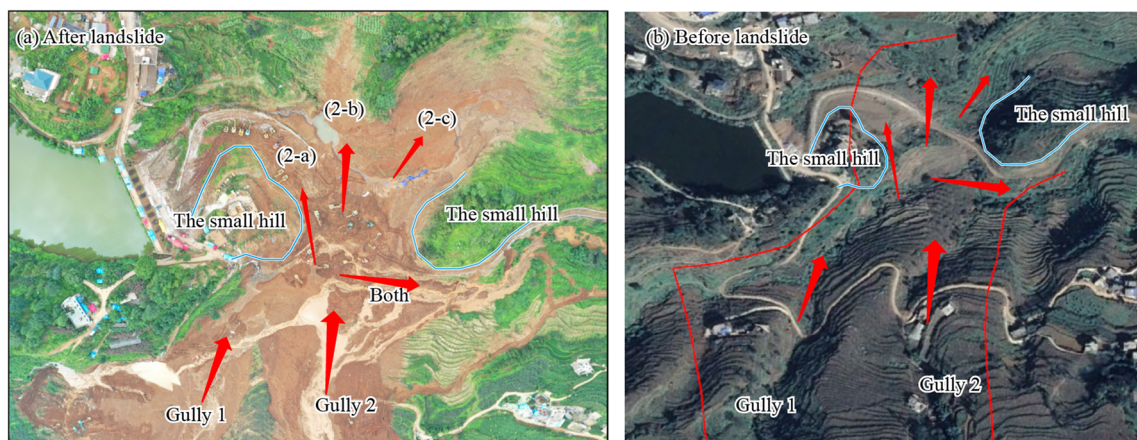

Fig. 14 Flowing, settling, and depositing process of the sliding body in the field as obtained by the simulated flow process: **a** after and **b** before the landslide
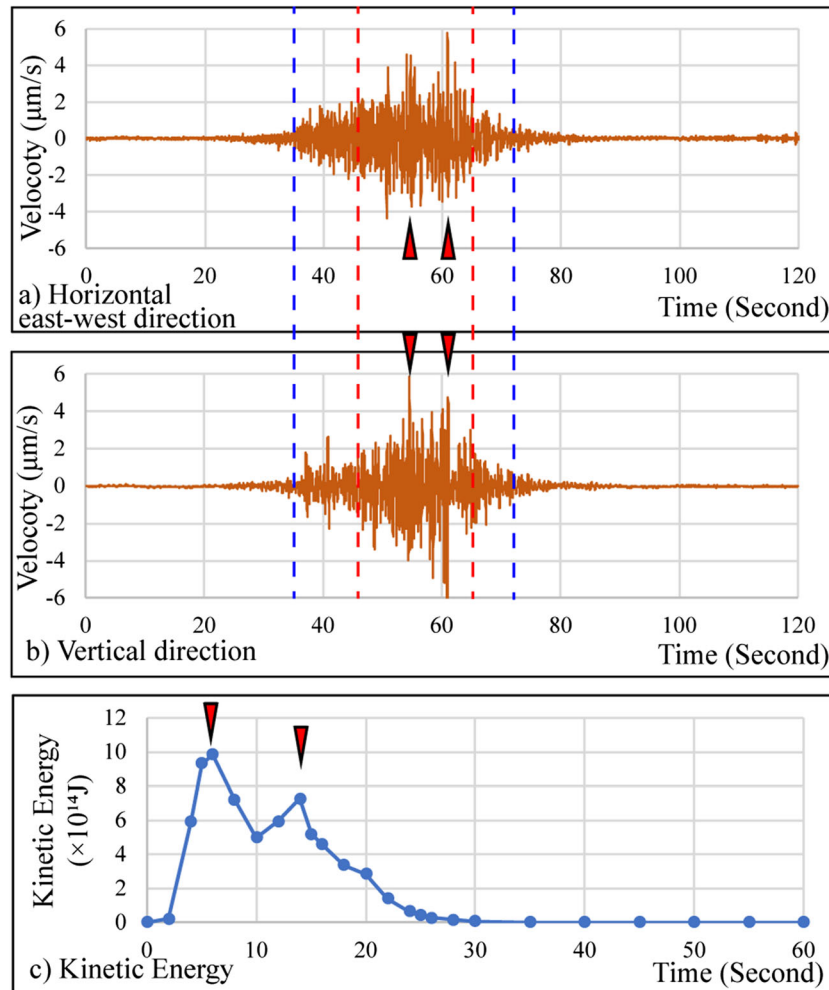
Fig. 15 a, **b** Landslide event recorded by seismic waves; **c** kinetic energy calculated from the numerical results

In summary, this work reproduced the entire movement process of a catastrophic landslide using a depth-averaged model, which provides a detailed reference for investigating other long-runout, high-speed, flow-like landslides. For flow-like landslide, the control of topography and the friction of slope surface have important influence on the movement process of landslides. In the area prone to flow-like landslide, it is of certain significance to guide the selection of construction site and avoid disaster loss.

References

Bouchut F, Westdickenberg M (2004) Gravity driven shallow water models for arbitrary topography. Commun Math Sci 2(3):359–389 https://projecteuclid.org/euclid.cms/1109868726

Castro-Orgaz O, Hutter K, Giraldez JV et al (2014) Nonhydrostatic granular flow over 3-D terrain: New Boussinesq-type gravity waves. J Geophys Res Earth Surf 120:1–28. https://doi.org/10.1002/2014JF003279

Denlinger RP, Iverson RM (2004) Granular avalanches across irregular three-dimensional terrain: 1. Theory and computation. J Geophys Res 109 (F1):F01014. https://doi.org/10.1029/2003JF000085

Ekstrom G, Stark C (2013) Simple scaling of catastrophic landslide dynamics. Science 339:1416–1419. https://doi.org/10.1126/science.1232887

Fan XM, Xu Q, Scaringi G, Dai L, Li W, Dong X, Zhu X, Pei X, Dai K, Havenith HB (2017) Failure mechanism and kinematics of the deadly June 24th 2017 Xinmo landslide, Maoxian, Sichuan, China. Landslides 14:2129–2146. https://doi.org/10.1007/s10346-017-0907-7

George DL, Iverson RM (2014) A depth-averaged debris-flow model that includes the effects of evolving dilatancy. II. Numerical predictions and experimental tests. Proc R Soc A Math Phys Eng Sci 470(20130820). https://doi.org/10.1098/rspa.2013.0819

Gray JMNT, Edwards AN (2014) A depth-averaged μ(I)-rheology for shallow granular free-surface flows. J Fluid Mech 755:503–534. https://doi.org/10.1017/jfm.2014.450
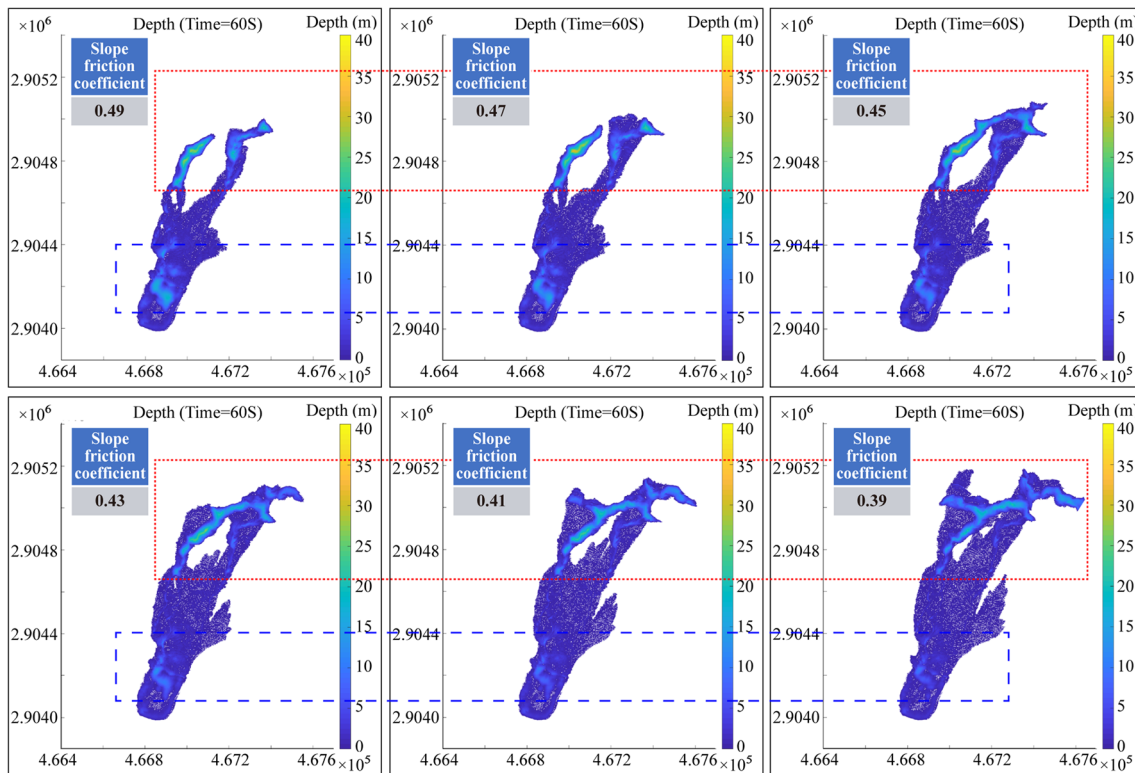
Fig. 16 Comparing the final morphologies the landslide predicted with different friction coefficients for the slope surface

Gray JMNT, Wieland M, Hutter K (1999) Gravity-driven free surface flow of granular avalanches over complex basal topography. Proc R Soc A Math Phys Eng Sci 455:1841–1874. https://doi.org/10.1098/rspa.1999.0383

Guizhou Meteorological Bureau (2019) Liupanshui: check the past meteorological data of the landslide site, and the chief forecasters of the municipal meteorological bureau study the future weather trend together. https://gz.cma.gov.cn/xwzx/qxyw/201907/t20190725_939861.html. Accessed 25 July 2009 (in Chinese)

Guo J, Yi S, Yin Y, Cui Y, Qin M, Li T, Wang C (2020) The effect of topography on landslide kinematics: a case study of the Jichang town landslide in Guizhou, China. Landslides 17:959–973. https://doi.org/10.1007/s10346-019-01339-9

Guthrie RH, Friele P, Allstadt K, Roberts N, Evans SG, Delaney KB, Roche D, Clague JJ, Jakob M (2012) The 6 August 2010 Mount Meager rock slide-debris flow, Coast Mountains, British Columbia: characteristics, dynamics, and implications for hazard and risk assessment. Nat Hazards Earth Syst Sci 12:1277–1294. https://doi.org/10.5194/nhess-12-1277-2012

Hergarten S, Robl J (2015) Modelling rapid mass movements using the shallow water equations in Cartesian coordinates. Nat Hazards Earth Syst Sci 15(3):671–685. https://doi.org/10.5194/nhess-15-671-2015

Hu K, Wu C, Tang J, Pasuto A, Li Y, Yan S (2018) New understandings of the June 24th 2017 Xinmo landslide, Maoxian, Sichuan, China. Landslides 15:2465–2474. https://doi.org/10.1007/s10346-018-1073-2

Hungr O, Leroueil S, Picarelli L (2014) The Varnes classification of landslide types, an update. Landslides 11:167–194. https://doi.org/10.1007/s10346-013-0436-y

Iverson RM, George DL (2014) A depth-averaged debris-flow model that includes the effects of evolving dilatancy. I. Physical basis. Proc R Soc A Math Phys Eng Sci 470(20130819). https://doi.org/10.1098/rspa.2013.0819

Iverson RM, George DL, Allstadt K, Reid ME, Collins BD, Vallance JW, Schilling SP, Godt JW, Cannon CM, Magirl CS, Baum RL, Coe JA, Schulz WH, Bower JB (2015) Landslide mobility and hazards: implications of the 2014 Oso disaster. Earth Planet Sci Lett 412:197–208. https://doi.org/10.1016/j.epsl.2014.12.020

Juez C, Murillo J, García-Navarro P (2013) 2D simulation of granular flow over irregular steep slopes using global and local coordinates. J Comput Phys 255:166–204. https://doi.org/10.1016/j.jcp.2013.08.002

Legros F (2002) The mobility of long-runout landslides. Eng Geol 63(3–4):301–331. https://doi.org/10.1016/S0013-7952(01)00090-4

Mangeney A, Bouchut F, Thomas N, Vilotte JP, Bristeau MO (2007) Numerical modeling of self-channeling granular flows and of their levee-channel deposits. J Geophys Res Earth Surf 112:1–21. https://doi.org/10.1029/2006JF000469

Pouliquen O, Forterre Y (2002) Friction law for dense granular flows: application to the motion of a mass down a rough inclined plane 453:133-151. https://doi.org/10.1017/S0022112001006796

Pudasaini SP, Hutter K (2003) Rapid shear flows of dry granular masses down curved and twisted channels. J Fluid Mech 495:193–208. https://doi.org/10.1017/S0022112003006141

Pudasaini SP, Hutter K, Hsiau SS, Tai SC, Wang Y, Katzenbach R (2007) Rapid flow of dry granular materials down inclined chutes impinging on rigid walls. Phys Fluids 19(5):053302. https://doi.org/10.1063/1.2726885

Savage SB, Hutter K (1989) The motion of a finite mass of granular material down a rough incline. J Fluid Mech 199:177–215. https://doi.org/10.1017/S0022112089000340

Scheidegger AE (1973) On the prediction of the reach and velocity of catastrophic landslides. Rock Mech Rock Eng 5:11–40. https://doi.org/10.1007/BF01301796

Watkins JA, Ehlmann BL, Yin A (2015) Long-runout landslides and the long-lasting effects of early water activity on Mars. Geology 43(2):107–110. https://doi.org/10.1130/G36215.1

Xia X, Liang QH (2018) A new depth-averaged model for flow-like landslides over complex terrains with curvatures and steep slopes. Eng Geol 234:174–191. https://doi.org/10.1016/j.enggeo.2018.01.011

Xia X, Liang Q, Ming X (2019) A full-scale fluvial flood modelling framework based on a high-performance integrated hydrodynamic modelling system (HiPIMS). Adv Water Resour 132:103392

Yin Y, Xing A (2012) Aerodynamic modeling of the Yigong gigantic rock slide-debris avalanche, Tibet, China. Bull Eng Geol Environ 71(1):149–160. https://doi.org/10.1007/s10064-011-0348-9

Zhang Z, He S, Liu W et al (2019) Source characteristics and dynamics of the October 2018 Baige landslide revealed by broadband seismograms. Landslides 16:777–785. https://doi.org/10.1007/s10346-019-01145-3

Zhao W, Wang R, Liu X, Ju N, Xie M (2020) Field survey of a catastrophic high-speed long-runout landslide in Jichang Town, Shuicheng County, Guizhou, China, on July 23, 2019. Landslides 17:1415–1427. https://doi.org/10.1007/s10346-020-01380-z

Zhou J, Cui P, Hao M (2016) Comprehensive analyses of the initiation and entrainment processes of the 2000 Yigong catastrophic landslide in Tibet, China. Landslides 13:39–54. https://doi.org/10.1007/s10346-014-0553-2

W. Zhao (✉) · **N. Ju**
State Key Laboratory of Geohazard Prevention and Geoenvironment Protection,
Chengdu University of Technology,
Chengdu, 610059, Sichuan, China
Email: zhaoweihua15@cdut.edu.cn

X. Xia · **X. Su** · **Q. Liang**
School of Architecture, Building and Civil Engineering,
Loughborough University,
LeicestershireLE113TU, U.K.

X. Liu
Guizhou Technical Center for Geological Hazards Emergency,
Guiyang, 550004, Guizhou, China